5.2 Geodetic and Oceanographic Applications of Satellite Altimetry

R. E. Cheney, B. C. Douglas, D. C. McAdoo and D. T. Sandwell

National Geodetic Survey, Charting and Geodetic Services, National Ocean Service, NOAA, Rockville, Maryland, USA

I. Introduction

The form of the ocean surface, or "sea surface topography", has both constant and time-varying components. The principal constant component is caused by the geopotential, which produces deviations of the sea surface from a best-fitting ellipsoid of revolution of up to 100 m. Tides and geostrophic currents cause additional smaller (~1 m) deviations from the level surface produced by the geopotential. As we shall see, for most marine geophysical applications, the purely oceanographic effects can be neglected and the sea surface assumed level.

Time-varying changes of sea surface topography, although small compared to the permanent undulations created by the geopotential, are large compared to the accuracy (a few centimeters) of a satellite altimeter. In addition, sea height variability can be observed independent of geoid

SPACE GEODESY AND GEODYNAMICS
ISBN 0-12-057840-9

topography either at intersections ("crossovers") of the satellite ground track or on repeating (collinear) tracks. Both measures of variability have been used successfully, but the latter is preferred because a more consistent and uniform time series of observations is realized.

Sea surface profiles are obtained by accurately determining the round trip travel time of the microwave pulse between the satellite and ocean surface. But the pulse is also affected by the sea surface. For example, crests of waves scatter energy, and troughs focus it. Thus the greater the sea state, the more the pulse shape is distorted. The very short-wavelength capillary waves caused by the wind have a different effect, scattering energy and reducing the amplitude of the return pulse as wind speed increases. Suitable algorithms exist that can be used to determine sea state and wind speed from the form and strength of the return pulse. Comprehensive discussions of all applications of altimeter data from GEOS-3 and SEASAT have been collected in several volumes of the *Journal of Geophysical Research* (Vol. 84, no. B8, 1979; Vol. 87, no. C5, 1982; Vol. 88, no. C3, 1983), and a complete bibliography can be found in Brown and Cheney (1983).

In addition to the obvious problems of interpreting altimeter data, there is the geodetic problem of determining the trajectory of the satellite, because altimeter profiles are taken relative to the satellite path which varies in its own unique way. Thus interpreting altimeter data cannot be separated from the problem of satellite tracking and orbit determination. Indeed it is for this reason that there is such a large representation of satellite geodesists in the community that analyzes satellite altimeter data.

II. Geometry of Satellite Altimeter Observations

An altimetric satellite, by the nature of its mission, has severe limitations placed on the parameters of its orbit. It must not be at so low an altitude that atmospheric drag significantly perturbs the orbit (<800 km) nor so high (>1500 km) that an extraordinary amount of power is required by the altimeter. In addition, the inclination of the orbit to the equator must be high to observe as much of the ocean surface as possible, but at the same time low enough that both components of the surface slope are accurately observed. A further complication arises from certain high inclinations where the orbital precession rate leads to aliasing of tidal and other perturbations on the orbit with sought-after frequencies of ocean circulation. These limitations mean that the orbital frequency will be 13–14 rev. per day and the inclination well away from sun-synchronous.

The planned NASA TOPEX (topography experiment) satellite (National Aeronautics and Space Administration, 1981) illustrates well the above

considerations. The inclination of the orbit to the equator will be approximately 63.5° to prevent aliasing of solar pressure and tidal perturbations with seasonal variations of the general circulation. An altitude of approximately 1300 km was chosen to place the satellite at a height where drag effects are very small, but low enough for reasonable power requirements for the altimeter.

Another constraint on the orbit of an altimeter satellite occurs because an oceanographic satellite must make repeated measurements of the surface. Although such observations occur at intersections of the groundtrack for any orbit, these "crossovers" do not occur spatially or temporally in a manner suitable for spectral analyses. Intersections occur nearly at integral multiples of an orbital period, and are not uniformly distributed. For example, a high-inclination orbit will produce many intersections in the polar regions, but few at low latitudes. Thus the preferred sampling scheme involves repeating (collinear) groundtracks. However, a tradeoff exists here between temporal and spatial sampling because a rapid time sampling leads to coarse geographic coverage, and vice versa. For example, the 3-day repeat cycle used by SEASAT during its last month of operation produced a groundtrack spacing of 930 km at the equator. The TOPEX groundtrack will repeat every 10 days, yielding 215-km spacing of the tracks.

III. Satellite Orbit Determination

A satellite altimeter mission places extreme requirements on the accuracy to which the path of the satellite must be known. Variations in ocean dynamic height of a few centimeters over wavelength scales from a few tens of kilometers to entire ocean basins need to be observed accurately. Since altimetric profiles of the ocean surface are taken relative to the satellite trajectory, the maximum benefit of a satellite altimeter mission will be obtained only if the trajectory of the satellite is known to an accuracy approaching that of the altimeter itself.

The problem of satellite orbit determination for the SEASAT altimeter satellite was extensively covered in a special issue of the *Journal of the Astronautical Sciences* (Vol. 28. no. 4, 1980). The results of these studies confirmed what has long been known about error in position of a satellite. That is, the error is very systematic, being primarily concentrated at a frequency of one per revolution, with power falling off very rapidly at both lower and higher frequencies. Thus at the wavelength associated with mesoscale oceanographic phenomena or statically supported loads on the lithosphere (a few hundred kilometers), the error in the satellite altitude is insignificant. It is for this reason that the most successful applications of

GEOS-3 and SEASAT data were in computing mesoscale variability from repeated profiles of data, or geoidal undulations at similar small scales. Attempts to compute ocean circulation basin-scale features were less successful, although still interesting, as will be seen later. The SEASAT project computed the radial position (and hence altitude) of the satellite to an accuracy of 60–70 cm (Marsh and Williamson, 1980). Geometric algorithms utilizing the groundtrack crossovers to constrain the trajectory were able to further reduce this figure by at least one-half (Douglas *et al.*, 1984).

The problem of satellite orbit determination is essentially one of reconciling observations made of a *component* of the satellite's position or velocity from a network of stations with the integrated effects of the forces on the satellite. Unlike the situation for aircraft or ships, complete position fixes are never obtained. The orbit determination problem involves computing a continuous trajectory that is simultaneously consistent with the tracking data and satellite equations of motion. The latter equations are of course well known, but some force model parameters used to compute the accelerations of the satellite are in varying degrees uncertain. The principal errors in the force model are uncertainty of the geopotential and atmospheric drag. Significant effects of drag can be eliminated either by placing the altimetric satellite at a sufficiently high altitude or employing surface-force compensation devices on the satellite. The problem of the geopotential is much more difficult. This matter is being addressed by major efforts at several organizations in the United States and abroad. If the flight program envisioned as a part of the NASA Geopotential Research Mission (GRM) is undertaken, the effect of the error of the geopotential on satellite orbit determination will be entirely eliminated. In the case of TOPEX, precision orbits at the decimeter level of accuracy will be obtained by employing a world-wide network of improved TRANET Doppler tracking stations providing very nearly continuous coverage of the orbit.

IV. Marine Gravity and Geophysics

Undulations of the mean sea surface, or the (nearly identical) geoid, are caused primarily by lateral density inhomogeneities within the Earth. These mass anomalies are physically supported by deviatoric stresses arising either from convective motions of the viscous mantle or from static loads on the rigid lithosphere. Mantle-wide convection maintains many of the longer-wavelength ($>10^6$ m), larger-amplitude (>10 m) geoid undulations (Kaula, 1972). Indeed, a number of studies point out the high correlation between geoid undulations and surface manifestations of mantle convection such as spreading ridges, subduction zones and hot-spot swells (Haxby and

Turcotte, 1978; Sandwell and Schubert, 1980; Griggs, 1972; Hager, 1984; Crough and Jurdy, 1980).

Although the geoid is dominated by these longer-wavelength undulations, much information is contained in the shorter-wavelength ($\ll 10^6$ m) signals. These primarily originate from density anomalies within the lithosphere. In all but a few extreme cases, shorter-wavelength geoid undulations are highly correlated with seafloor topography. The high resolution and accuracy of the SEASAT radar altimeter provides a global view of these shorter wavelength geoid undulations.

The most prominent seafloor features reflected in the sea-surface topography are trenches, fracture zones, large seamounts and spreading ridges. Examples of SEASAT profiles across trenches and oceanic fracture zones are presented below along with physical models of these features. Other examples of altimeter profiles over seamounts and spreading ridges are presented in papers by Haxby and Turcotte (1978) and Watts and Ribe (1984).

The shape of the marine geoid at shorter spatial wavelengths is predominantly a smoothed, attenuated version of seafloor topography (see Chapman, 1979). It is, therefore, not surprising that deep-ocean trenches (and the outer rises which flank them) appear in the marine geoid and are readily observed by satellite altimeters. In fact, the deep-ocean trenches represent the largest amplitude undulations in the marine geoid exclusive of very long (>4000 km) wavelengths. The Aleutian trench, for example, contributes 15 m of relief. Trenches manifest themselves so clearly in the geoid because they are paramount bathymetric features and they are not, to a large degree, isostatically compensated (Vening Meinesz, 1964).

Outer rises lying just seaward of most deep-ocean trenches also are isostatically uncompensated features (Watts and Talwani, 1974; McAdoo and Martin, 1984). These have wavelengths (transverse to trench axes) of several hundred kilometers and contribute as much as 6 m of relief to the marine geoid. They are attributable to flexure of the oceanic lithosphere prior to subduction. This flexure is generally modeled by representing the oceanic lithospheric as an end-loaded elastic plate (Fig. 1). This elastic model of lithospheric deflection predicts the topographic shape for the outer rise and outer wall of the trench. It can be extended to predict concomitant geoid undulations. An approximate, analytical expression for these predicted geoid undulations is derived in McAdoo and Martin (1984). This enables predicted geoid undulations to be compared with individual SEASAT or other satellite altimeter passes over outer rises. First, passes are high-pass filtered by removing a reference geoid. By using the method of least squares, elastic model parameters such as flexural wavelength, can be estimated for each altimeter pass. Two such SEASAT passes, an ascending pass over the

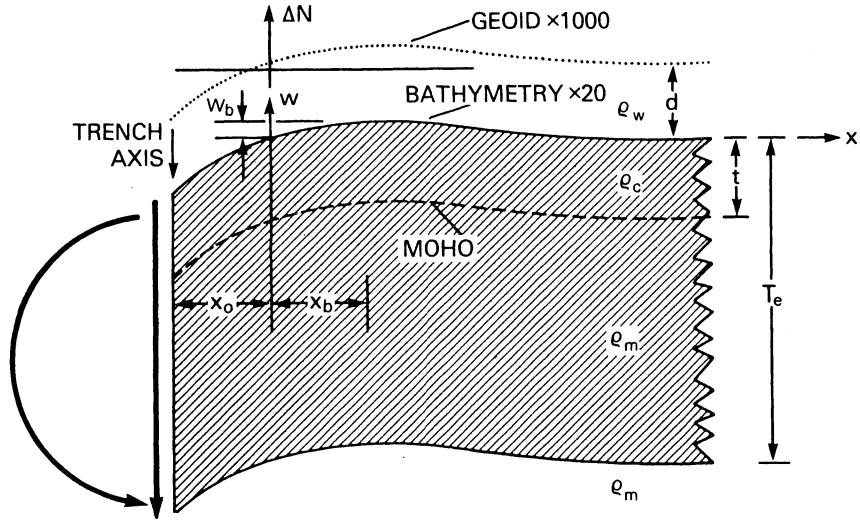

Fig. 1. Model of end-loaded elastic lithospheric plate overlying a fluid-like asthenospheric substrate. Crust and lithosphere deflect as a unit. Model outputs include seafloor deflection profile, $w(x)$ and concomitant profile of geoid heights, $N(x)$ [From McAdoo and Martin (1984).]

southern Mariana Trench and a descending pass across the South Sandwich Trench, are shown in Fig. 2. Note that available bathymetric data across these trenches are not suitable for studies such as this. Estimates of flexural wavelength can be converted to estimates of lithospheric thickness. In McAdoo and Martin (1984) and McAdoo *et al.*, (1985), SEASAT altimeter data over various outer rises are used to demonstrate that the mechanical lithosphere thickens with age in a manner consistent wth established thermal models (e.g. Parsons and Sclater, 1977), and can achieve a thickness as great as 60 or 70 km. So, SEASAT data significantly augment available information concerning the shapes of outer rises and regional variations in the thickness of the lithosphere.

In general, satellite altimeter data are particularly suited to geophysical studies of long, linear features like trenches, outer rises or fracture zones because these data enjoy the advantage of geoidal representation in which unmodeled, local, short-wavelength effects such as those of seamounts are attenuated.

Fracture zones are linear scars in the seafloor produced by transform faulting (Wilson, 1965). Topography along their inactive segments consists of long ridges, troughs and scarps separating regions of different depth (Menard and Atwater, 1969). Figure 3 shows how fracture zones (FZs) are formed as part of the seafloor spreading process. Spreading ridges generally

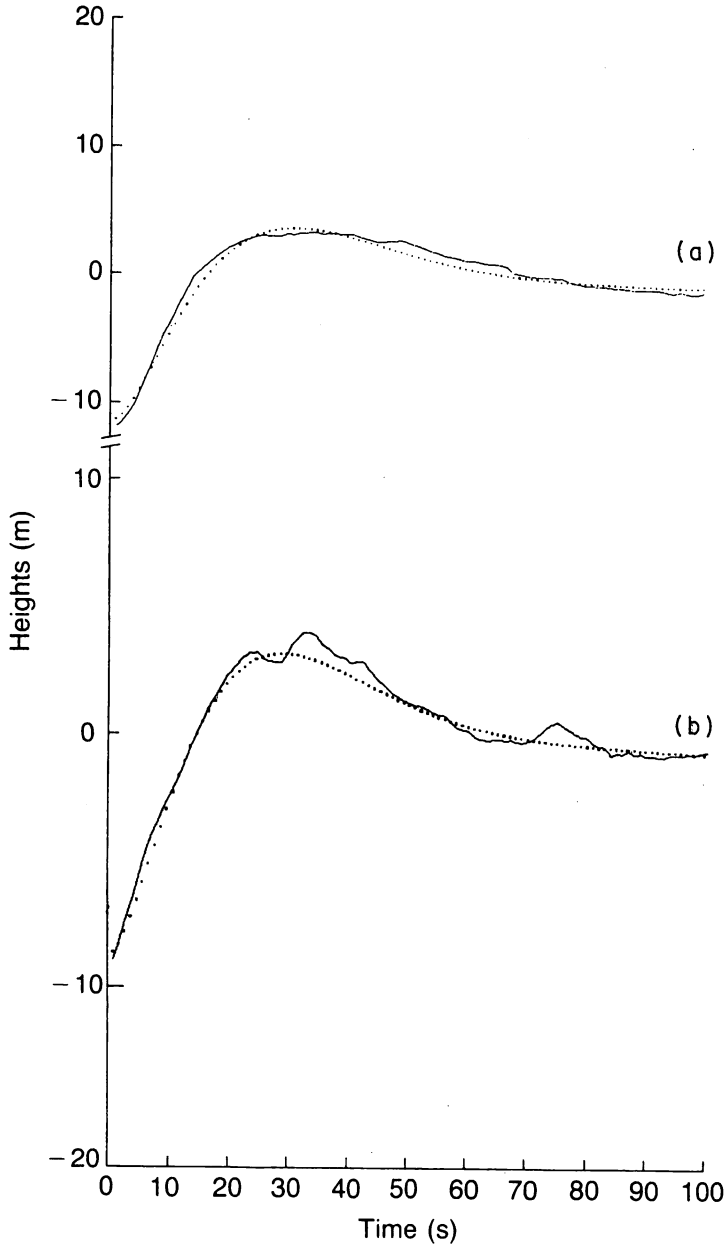

Fig. 2. Individual SEASAT passes (low-cut filtered) across two trenches. Shown as dotted curves are best-fitting geoid profiles generated by an elastic lithosphere model. (a) South Sandwich Trench, $\phi = -55.60°$, $\lambda = 333.85°$, Rev = 468, $\alpha = 105.5 \pm 4.3$, $W_0 = 1975 \pm 94$. (b) Southern Mariana Trench, $\phi = 10.85°$, $\lambda = 140.92°$, Rev = 829, $\alpha = 103.1 \pm 5.3$, $W_0 = 1683 \pm 10$.

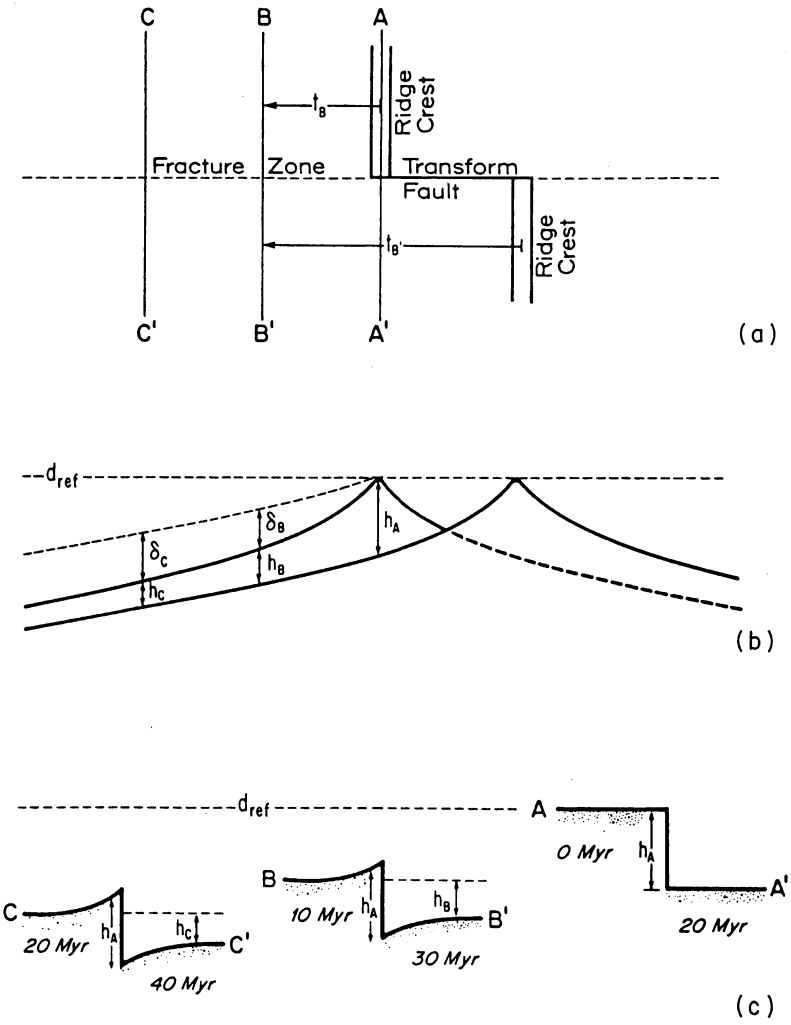

Fig. 3. Evolution of a FZ. (a) Spreading ridges offset by a transform fault. No relative motion occurs across the FZ. (b) The overall depth offset across the fracture zone decreases with age. The scarp at the ridge–transform intersection remains constant at h_A. (c) The ridge and trough flexural topography develops as the FZ ages.

consist of short segments (50–500 km) offset by transform faults. Strike-slip motion occurs along the transform fault as shown in the top of Fig. 3, producing fractures in the seafloor. Once the lithosphere migrates beyond the intersection of the spreading ridge with the transform fault, the two

sections of lithosphere move at the same rate and eventually become welded together. The fractured seafloor remains along this older section of the FZ although no new fractures develop.

The general increase in seafloor depth with increasing seafloor age produces additional topography in the vicinity of a FZ. As shown in Fig. 3 (Sandwell and Schubert, 1982), a FZ separates newly created lithosphere (0 Myr) from older lithosphere (20 Myr) (see A′-A′). As these two segments of lithosphere move away from the ridge crest from A-A′ to B-B′, the depth far from the FZ on the younger lithospheric segment increases at a higher rate than the depth far from the FZ on the older segment (Menard and Atwater, 1969; Delong *et al.*, 1977; Sibuet and Mascle, 1978). This effect is shown by the two subsidence curves in the middle of Fig. 3. Since the lithosphere is welded at the ridge-transform intersection, the FZ does not slip during its evolution. Therefore the height of the scarp will remain at its initial value h_A. The lithosphere must flex to satisfy both of these requirements as shown in the lower portion of Fig. 3.

Results from a physical model for the thermomechanical evolution of a FZ are shown in Fig. 4 (Sandwell, 1984). Figure 4(a) shows the development of the ridge and trough topography across a large age-offset FZ (i.e. 20 Ma age offset). Since the younger lithosphere subsides at a higher rate than the older lithosphere, the ridge and trough signature develops in just a few million years. This flexural topography extends to about 100 km on either side of the FZ.

The same model is used to predict the geoid step (Fig. 4(c)) and the geoid slope (Fig. 4(b)) across a FZ. The geoid step has an amplitude of 3 m while maximum geoid slopes (i.e. deflections of the vertical) are 80 μrad. As the FZ evolves the geoid step becomes complex, reflecting the development of the ridge and trough topography. The deflection of the vertical, rather than the geoid profile, is compared with the data because differentiation of the SEASAT profile removes the long-wavelength, large-amplitude components of the geoid that are associated with density anomalies in the mantle.

Large values of the deflection of the vertical (~50 μrad = 10 arcsec) occur along the Udintsev FZ because of its large age offset (~18 Ma, Weissel *et al.*, 1977). Examples of along-track deflection of the vertical profiles, computed by differentiating a subset of descending SEASAT altimeter passes, are shown in Fig. 5. On this projection, the Heezen, Tharp and Udintsev transform faults are heavy horizontal lines whereas segments of the Pacific-Antarctic spreading ridge are vertical heavy lines. Deflections of the vertical along the Udintsev FZ (i.e. filled profiles in Fig. 5) show a simple systematic pattern. At the midpoint between the two spreading ridges, a positive peak lies to the north of the transform fault while a negative peak lies to the

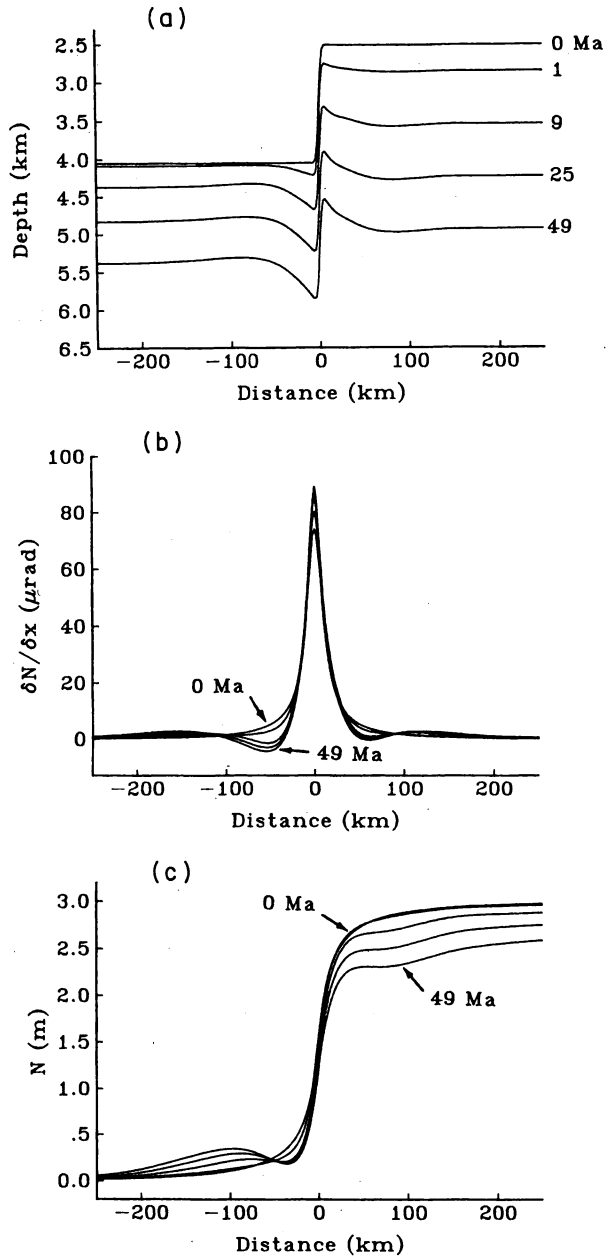

Fig. 4. Evolution of a FZ (20 Ma age offset) from a thermomechanical model. (a) Topography within a few million years flexural ridges and troughs develop. (b) Deflection of the vertical peak retains its high initial value reflecting the persistence of the bathymetric scarp. (c) Geoid step changes in shape but not in overall amplitude as the FZ ages. [Sandwell (1984).]

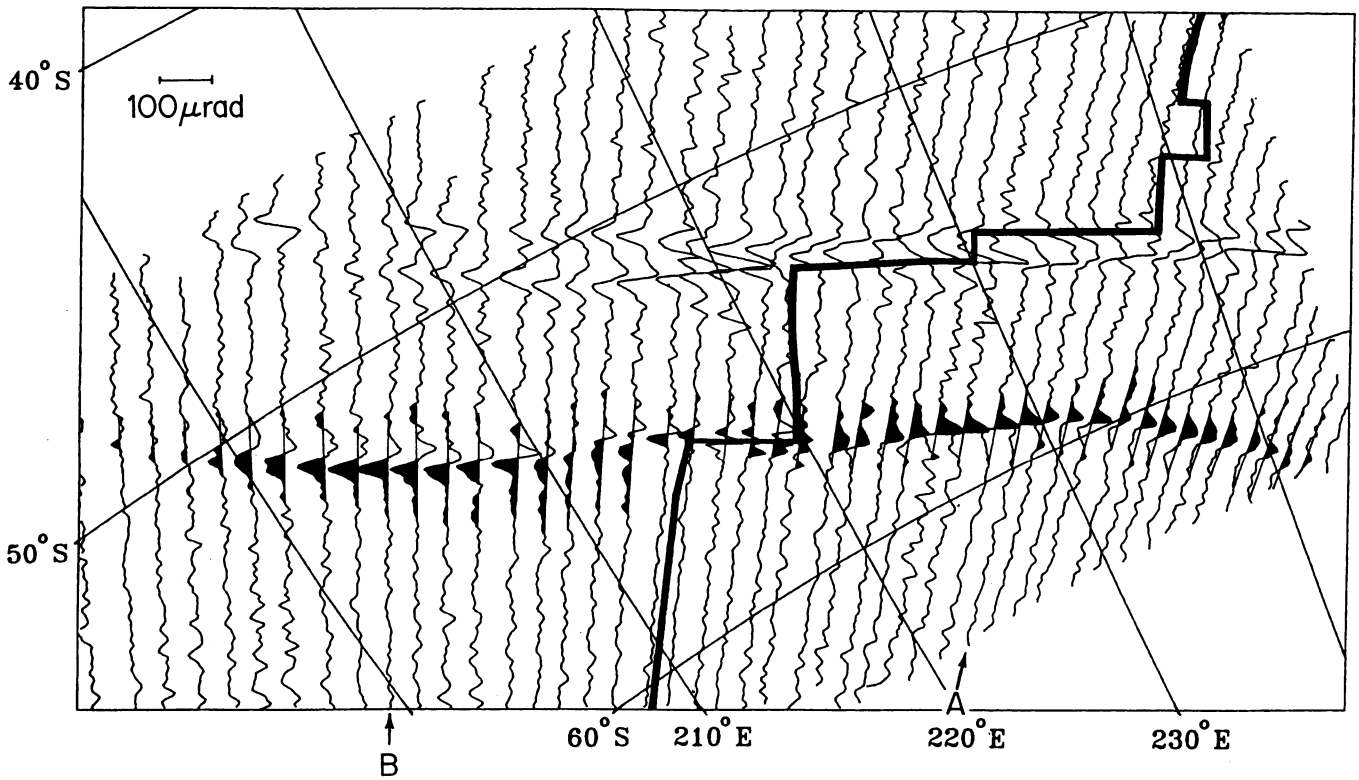

Fig. 5. Along-track deflection of the vertical profiles from differentiated SEASAT altimeter passes. Map projection is oblique Mercator where pole is the relative rotation axis between the Pacific and Antarctic plates. The plate boundary (heavy line) consists of spreading ridges (vertical lines) and transform faults (horizontal lines). Highlighted peaks reveal the characteristic signature of the major age-offset Udintsev FZ.

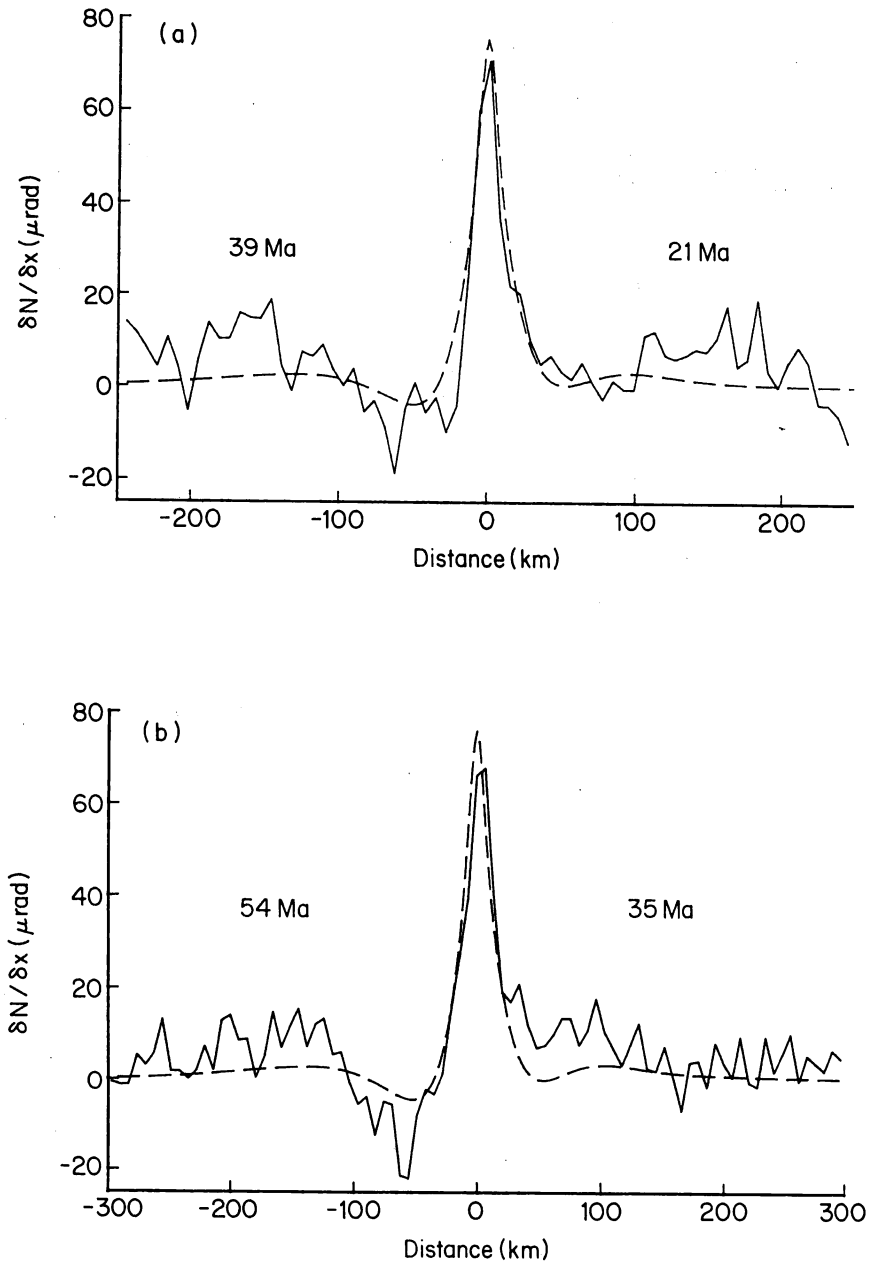

Fig. 6. Deflection of the vertical profiles across the Udintsev FZ (solid curves). Predictions of thermomechanical model (dashed curves). Locations of profiles (a) and (b) are shown in Fig. 7.

south. At the left ridge-transform intersection there is only a positive peak. Further to the left, along the inactive portion of the FZ, there is a positive peak centered above the FZ with a negative sidelobe on the older side. An analogous pattern occurs along the right inactive FZ segment. Thus, along all inactive portions of the Udintsev FZ there is a prominent sidelobe on the older side with a small or absent sidelobe on the younger side.

Two features of the deflection profiles across the Udintsev FZ support the flexure model of a FZ. The first is the persistence of the deflection of the vertical signature along older portions of the Udintsev FZ. This signal persists to at least 60 Ma where it diminishes because of a decrease in age offset (Weissel, personal communication, 1983). The second confirmation of the flexure model is the apparent asymmetry in deflection of the vertical.

Quantitative agreements between model profiles and observed profiles are shown in Fig. 6. The locations of the two profiles are marked in Fig. 5. Profile A was inverted and replotted (solid curve) along with the model prediction (dashed curve). For both profiles, the model matches the data fairly well although there are short-wavelength variations in the data that cannot be fit by the model. The model agrees equally well with about half of the other profiles shown in Fig. 5. Disagreements of the model with the other profiles could be due to crustal thickness variations or deviations of the thermal structure from the boundary layer cooling model.

V. Mesoscale Variability

Geostrophic surface currents are maintained by horizontal pressure gradients, and manifested as sea surface slopes relative to the geoid. While it is difficult to separate this dynamic component of sea height from the static geoid signal, an altimeter can readily detect time-dependent variations of height. The most energetic fluctuations have typical scales of 100–300 km and are attributable to the ocean eddy field (meandering of narrow currents and migration of detached vortices). Study of the oceanic eddy field is important because eddying motions are believed to be the dominant mechanism for transferring energy and momentum. Obtaining a basic description of global mesoscale eddy variability is thus fundamental to an improved understanding of ocean dynamics.

Computing mesoscale variability from altimeter data of course requires solving the problem of satellite orbit error. The method demonstrated here employs relatively short (1000–2000 km) profiles obtained along repeated ground tracks. Because orbit error has dominant scales many times larger than this, the relative error between two or more repeated passes can be

effectively removed as a linear trend. Analysis of profiles having identical tracks also eliminates any contribution from the geoid, enabling determination of time-variable sea height changes alone. An example is shown in Fig. 7. Two passes of GEOS-3 data were taken along the same track in the North Atlantic but at different times. A linear trend has been removed from each profile to eliminate the long-wavelength orbit error. Each pass contains the same geoid profile, as demonstrated by the close agreement over the seamount. However, at the location of the Gulf Stream there is a difference of 120 cm due to a meander or shift in the current's position. Mesoscale variability can therefore be detected with pairs of altimeter passes having the same track.

This procedure is most applicable to the GEOS-3 data which were collected in great volume in certain areas such as the North Atlantic. Even though GEOS-3 did not have an orbit which repeated exactly at specific intervals, it did produce many pairs of profiles along virtually the same ground tracks. Figure 8 is a map of sea height variability in the Gulf of Mexico and western North Atlantic derived from about 1000 collinear pairs of GEOS-3 data collected over 3.5 years. These results show peaks of variability created by the Loop Current in the Gulf of Mexico and by the

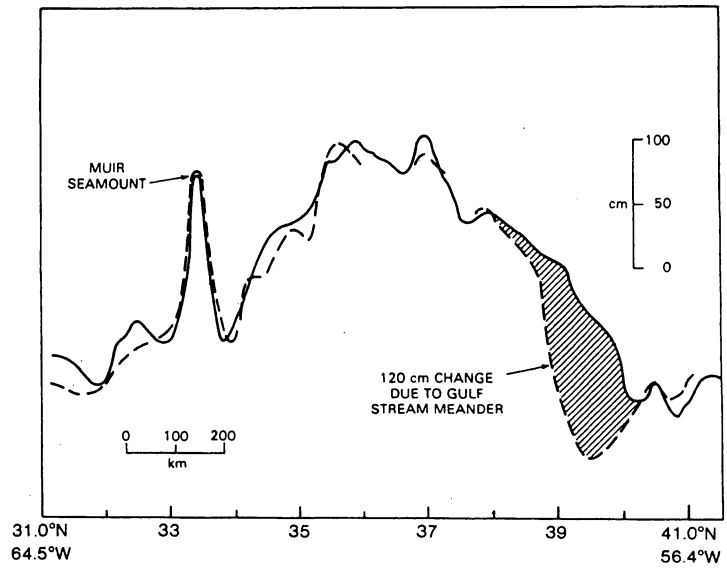

Fig. 7. A collinear pair of GEOS-3 altimeter profiles crossing the Muir Seamount north of Bermuda for 23 April 1977 (solid line) and 28 September 1977 (dashed line). Note the identical geoid undulation in the profiles at the position of the seamount. The shaded area is the change in height due to a meander of the Gulf Stream. [From Douglas *et al.* (1983).]

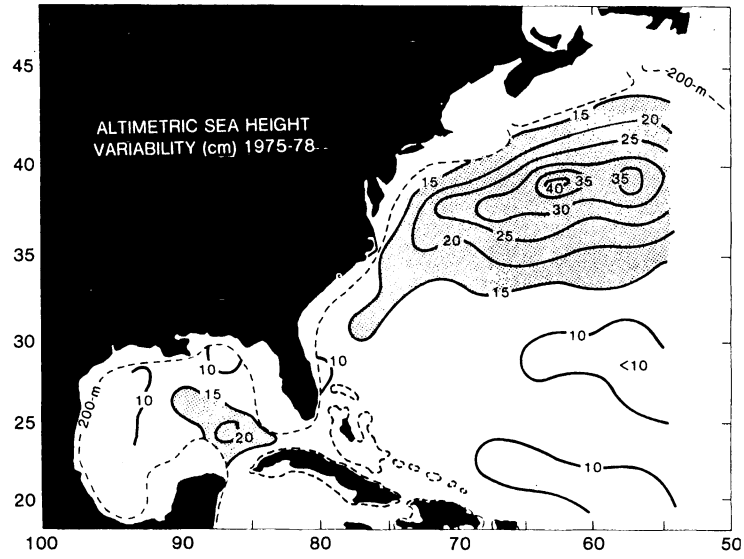

Fig. 8. Mesoscale sea surface height variability in centimeters computed from repeated pairs of GEOS-3 altimeter profiles during 1975–1978. Maximum values are associated with the Loop Current in the Gulf of Mexico and the Gulf Stream meander region downstream of Cape Hatteras. [From Douglas *et al.* (1983).]

Gulf Stream east of Cape Hatteras. The least energetic area is south of 35°N. A more detailed discussion of these results, including comparisons with similar maps derived from standard oceanographic data, has been published separately (Douglas *et al.*, 1983).

The technique of collinear differences has also been used to derive the global mesoscale variability from SEASAT altimeter data (Cheney *et al.*, 1983). In this case, statistics were derived not from pairs, but from nests of collinear profiles accumulated during a 25-day period when the ground track repeated at 3-day intervals. Variability was derived by computing the standard deviation of sea height every 7 km along the track from the series of eight or nine observations. Because of the relatively coarse cross-track grid described by the ground tracks (approximately 600 km at mid-latitudes), interpolation was required to compute values on a uniform global grid for contouring. The resulting map (Fig. 9) displays patterns consistent with our present understanding of the surface ocean circulation. In the North Pacific and the North Atlantic, the Kuroshio and Gulf Stream systems are represented as variability maxima extending 3000–4000 km into mid-ocean. The smoothing and interpolation process has damped their amplitudes down to about 10 cm from their actual along-track values of 20–30 cm, but they

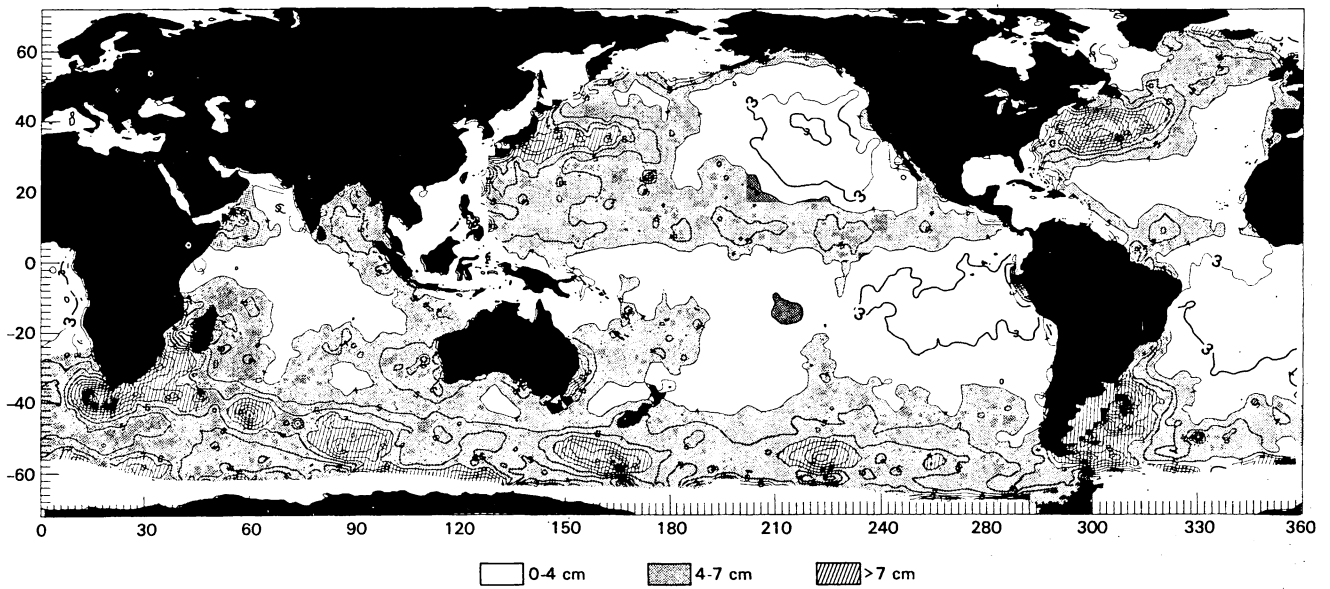

Fig. 9. Global mesoscale sea height variability measured by the SEASAT altimeter, 15 September–10 October, 1978. The North Atlantic and North Pacific are dominated by the highly energetic Gulf Stream and Kuroshio systems that extend seaward nearly 4000 km. In the Southern Hemisphere the Agulhas Current below Africa and the Falkland Brazil/Current confluence off South America are clearly apparent. High variability due to the Antarctic Circumpolar Current extends in a nearly continuous band through the polar oceans, with isolated maxima coinciding with major topographic ridges and plateaus. Owing to the predominance of values less than 4 cm in mid-ocean, the north equatorial current systems in both the Atlantic and Pacific can be seen as zonal bands of higher variability. [From Cheney *et al.* (1983).]

are still the dominant features of the Northern Hemisphere oceans. The North Equatorial Current systems are also associated with zonal bands of higher variability. The most prominent features in the Southern Hemisphere are the Agulhas Current off the tip of South Africa, the confluence of the Falkland and Brazil Currents east of Argentina and the Antarctic Circumpolar Current, represented as a series of variability maxima surrounding Antarctica. Because of westward intensification of the wind-driven ocean currents, higher variability is most prevalent in the western parts of the oceans. This is best demonstrated in the Atlantic where the Northern and Southern Hemispheres are nearly mirror images of each other. There is also a marked contrast between the highly variable western North Pacific and the quieter eastern basin, with the dividing line occurring near the Emperor seamount chain. This line of seamounts apparently acts as an efficient barrier to the high variability generated by the Kuroshio in the west. East-west asymmetry is characteristic of all oceans with values as small as 2–3 cm in the eastern parts of the major basins. Of all global variability values computed, 70% were less than 5 cm, 26% were in the 5–10 cm range, and only 4% were greater than 10 cm. It is this broad background of low variability that permits some of the equatorial currents to be detected even though their dynamic height signatures are relatively small (25 cm).

VI. Basin-scale Variability

The relationship of the ocean to climate is a key issue in contemporary oceanography. The ocean has the capacity to store large amounts of heat more readily than the atmosphere. We therefore need to understand the dynamics which influence the ocean-atmosphere balance, especially in the tropics where heat storage is large and time scales are short.

The El Niño–Southern Oscillation is one of the most dramatic air-sea interaction phenomena. During El Niño there is a collapse of the trade winds, resulting in sea-level changes of several decimeters over vast regions of the equatorial Pacific. In recent years, these sea-level changes have been well documented in the western Pacific by using island tide-gauge data (Wyrtki, 1979). This network has provided clear evidence of the very large scales of sea-level response during El Niño, particularly the pronounced 1982–1983 event when 40-cm monthly mean anomalies were observed. In contrast, El Niño signal is poorly observed in the eastern half of the Pacific where few islands are found.

No altimeter data are available from past El Niño years. However, SEASAT data can be used in simulations to test the ability of collinear altimeter data tracks to monitor El Niño events. The approach is similar to

that used for mesoscale variability except that longer profiles are required to detect the larger scales associated with El Niño.

El Niño sea-level signal extends along the equatorial ocean with meridional scales of a few thousand kilometers and zonal scales of up to 10,000 km. If we restrict our attention to individual altimeter tracks, we need only be concerned with detection of the relatively shorter-meridional signal since high-inclination satellite orbits cross the equator in a predominantly north-south direction.

As mentioned earlier in this chapter, the principle problem of satellite altimetry is error in determining the satellite's radial position. For SEASAT the magnitude of this error was 1-2 m with a dominant wavelength equal to the Earth's circumference. A secondary problem is removal of the tidal signal from altimetric profiles. At the scale of mesoscale variability, both effects can be eliminated simply by removing linear trends from profiles 1000-2000 km long. To observe sea-level changes with the much longer scales of El Niño, longer arcs are required, making the problem more difficult. The tide must be subtracted explicitly by using modeled heights, and orbit error must be approximated by a quadratic or higher-order trend.

In order to obtain a realistic test in the presence of radial orbit error, our simulation was performed using two adjacent 3-day arcs of SEASAT altimeter data taken in September, 1978. During this time the satellite groundtrack repeated every 3 days. Collinear altimetric profiles of sea surface topography 3 days apart should not show any large differences because the time scale is too small compared to any large-scale oceanographic phenomena other than the tides.

The first test was designed to evaluate how well orbit error and tidal signals could be removed. Data in the Pacific were used between 40°N and 40°S, yielding passes approximately 9500-km long (Fig. 10). To determine the sea-level change in 3 days, members of collinear pairs were subtracted to form difference profiles. Figure 11 shows an example for a collinear pair in the central Pacific. The upper profile is the difference between the two altimeter passes after removing only the modeled tide (Schwiderski, 1979). The large scale and amplitude of this curve are clearly indicative of radial orbit error. In the lower illustration, results of removing a quadratic trend from the difference profile are shown. The apparent change in sea level has been reduced by an order of magnitude to approximately 10 cm. (In computing the quadratic trend of the difference profile, values within 15° of the equator were not used. This was done to reduce damping of El Niño signal in the subsequent simulation.)

This procedure was followed for each of the Pacific collinear pairs, and mean sea height differences were accumulated in 10° blocks. Removal of the tide and a quadratic trend from each pair successfully reduced all block

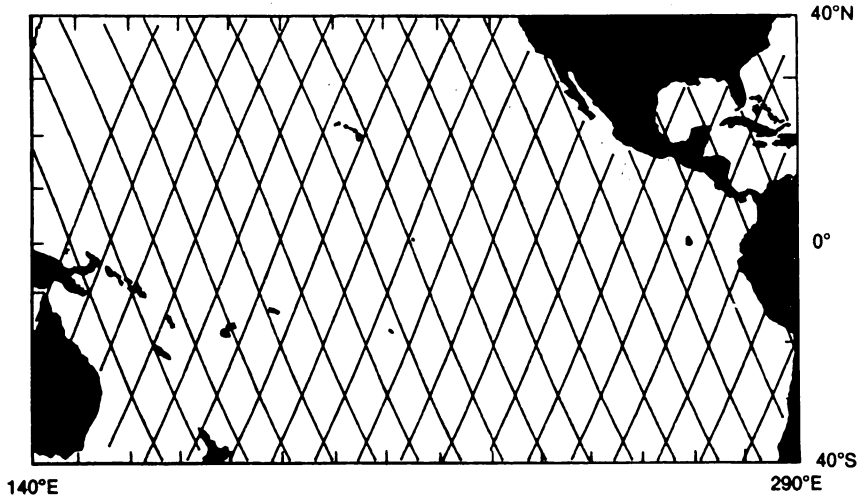

Fig. 10. SEASAT ground tracks during 23–28 September 1978. Two altimeter profiles, separated in the cross-track direction by only 0.4 km, were obtained along each track.

values to 10 cm or less, demonstrating that orbit error and tidal effects could be minimized over long arcs spanning the Pacific.

The El Niño simulation was performed based on modeled height anomalies. One of the 3-day sets of altimeter data was modified by the values shown in Fig. 12 to see if the signal could be recovered in the presence of 1-m orbit error. The signal was given a maximum amplitude of 40 cm at the equator, falling off to zero at 20°N and 20°S latitude. This is analogous to conditions that existed in December 1982 during the peak of the most pronounced El Niño event on record (Wyrtki, 1985). Of course, El Niño has never been accurately mapped in the eastern Pacific. In our model, we simply assumed a signal centered on the equator and symmetric about 160°W.

Figure 13 shows results of the simulation described previously. The model signal, present in one of the 3-day arcs, but not the other, was recovered virtually intact when the arcs were differenced. Peak amplitude was reduced by a few centimeters, and only 5 cm of noise was introduced in mid-latitude regions. The simulation demonstrates that orbit error can be removed from long arcs of altimeter data without aliasing El Niño signal. This technique can be made even more effective by incorporating tide-gauge observations in the solution as constraints wherever they are available. These form an important source of "surface truth" and strengthen the altimetric results.

Monitoring of basin-scale variability in the Pacific by using the method of collinear pairs should become a reality in 1986. The U.S. Navy altimeter

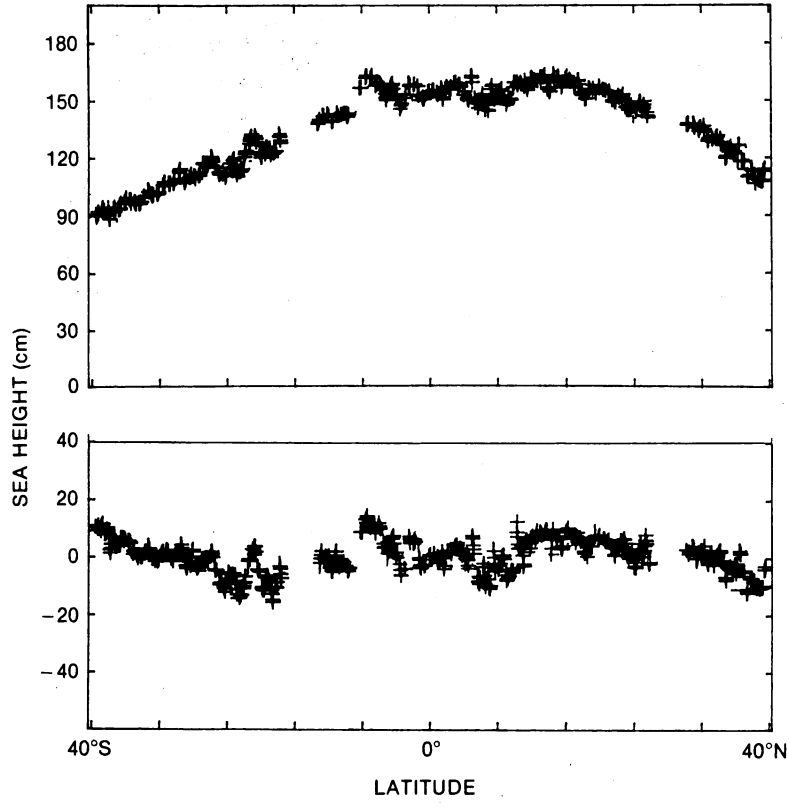

Fig. 11. SEASAT collinear pair differences in the central Pacific. (a) With only the tidal signal removed and (b) with the satellite height error eliminated by removal of a quadratic trend from the difference.

satellite GEOSAT will be launched in 1985. During the initial 18 months, sea surface topography will be mapped in great detail with a dense grid of closely spaced ground tracks. Few collinear passes will be generated during this portion of the mission, but after completion of the geodetic survey, the satellite will be placed in a 17-day repeat orbit. This will yield a spatial resolution of approximately 150 km globally and should provide a unique look at temporal sea-level variations on a variety of scales.

VII. Determining the Mean Circulation

Ultimately it is believed that satellite altimetry will contribute to determination of the general circulation of the oceans (the long-term mean movement of water). In order to accomplish this, advances will be required in gravity

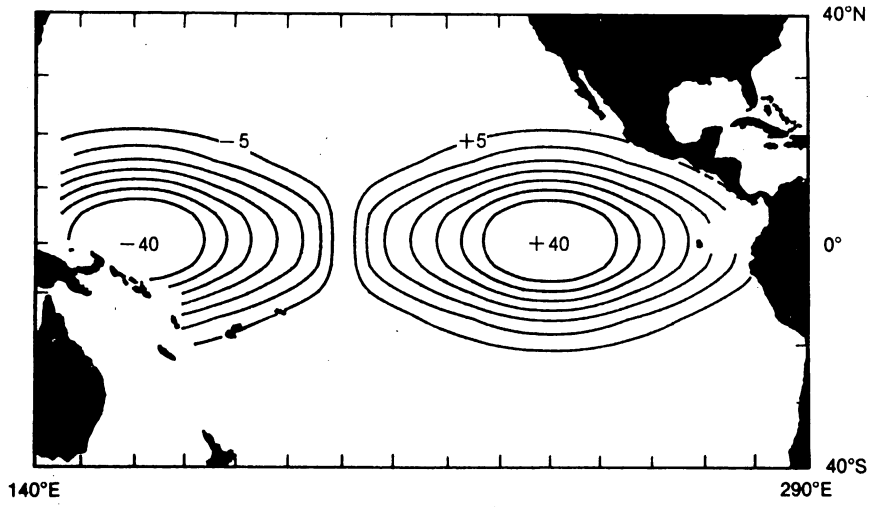

Fig. 12. Model of El Niño sea-level signal based on the 1982–1983 event. Values were assigned in 10° blocks and represent anomalies (in centimetres) from the long-term mean.

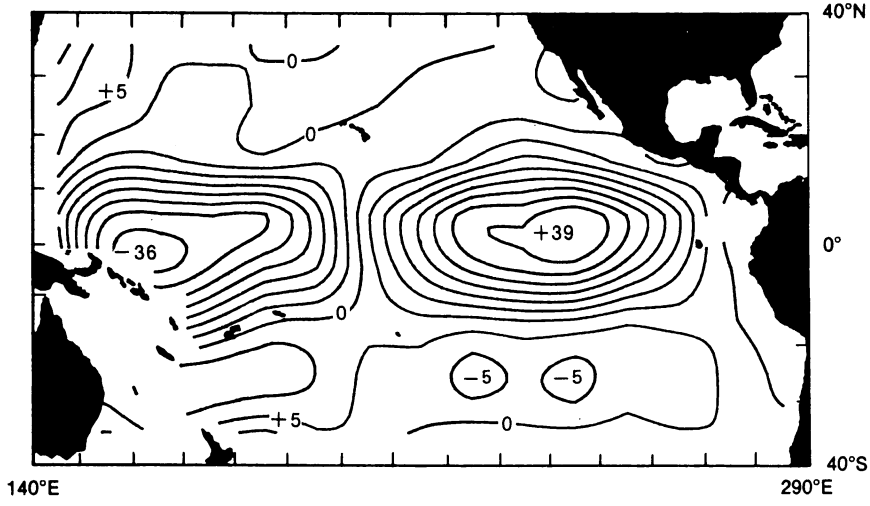

Fig. 13. Sea-level change (centimeters) recovered in a simulation using SEASAT altimeter data modified by model heights. Tides and orbit error were successfully removed over 9000-km arcs without significantly altering El Niño signal.

field modeling and orbit determination. At the present time, uncertainties in these two areas are probably too large for reliable mapping of surface circulation, although recently some surprisingly reasonable results have been obtained by using existing altimeter data and geoid models (Cheney and Marsh, 1982; Tai and Wunsch, 1983, 1984; Douglas *et al.*, 1984; Engelis, 1983). The example in Fig. 14 from Cheney and Marsh (1982) displays the difference between a global altimetric mean surface and a geoid model. The mean sea surface was computed using 1.5 years of GEOS-3 data and all 3 months of SEASAT data. No attempt was made to correct explicitly for long-wavelength radial orbit error; however, it was considered plausible that averaging over the 2-year span would produce a surface with good accuracy at the larger scales. The geoid model used was one generated to compute the most accurate orbits possible for SEASAT (Lerch *et al.*, 1982). The model, called PGS-S4, is based on the Goddard Earth Models (GEMS); it uses GEOS-3 and SEASAT altimeter data. The altimeter data, in particular, were weighted so that the higher-degree and -order terms of the geoid were improved (to 36,36). Sea heights for the global mean surface and the geoid model were both computed on a 1° grid.

The residual map in Fig. 14 was derived by subtracting the geoid from the altimetric surface. The residuals were then smoothed so that only features with scales greater than a few thousand kilometers were retained. (The filtering scheme has been described by Marsh and Martin, 1982. The 1° resolution surfaces were recomputed on a 5° grid by fitting a biquadratic surface to each point based on data within a 20° radius.) This smoothing was necessary for two reasons. First, the altimetric surface contains much more resolution and detail than the 36,36 geoid model. Second, the Goddard geoid models are highly accurate at long wavelengths, but degrade rapidly for terms greater than 6,6 (Wagner and Lerch, 1978). Thus these geoid models can only be used to derive the largest scales of ocean circulation.

The residual sea height map in Fig. 14 may be evaluated through comparison with maps of dynamic height calculated from shipboard measurements of temperature and salinity, e.g. those by Levitus (1982). There are many features of the altimetric solution that appear realistic. Sea height is 1–2 m higher at low latitudes than in subpolar seas. This establishes the well-known anticyclonic gyres in the major ocean basins. The simple fact that these gyres have the correct sense is highly encouraging. Details of their locations and magnitudes are of secondary importance. For example, in the altimetric solution, the North Pacific gyre is centered near Hawaii, while oceanographic charts show it more properly located south of Japan. Considering orbit and geoid uncertainties, such discrepancies are not unexpected. The altimetric solution does contain a strong, continuous current in the southern oceans much like the Antarctic Circumpolar Current. The

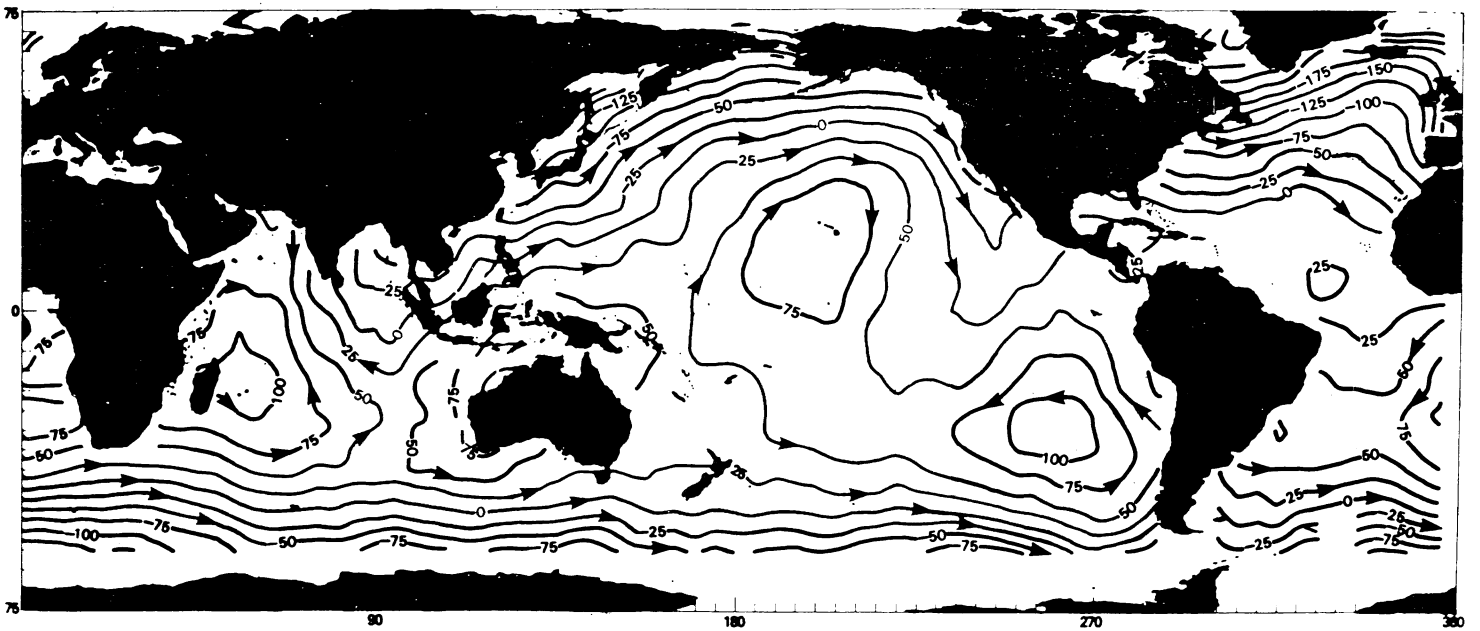

Fig. 14. Dynamic topography determined from altimetry. Contours in centimeters represent the difference between a long-term mean sea surface and a global geoid model. The surface consists of 1.5 years of GEOS-3 data plus all existing SEASAT altimetry. The geoid model, called PGS-S4 is based on a combination of satellite observational data, surface gravity, and also altimeter data. Both surfaces were smoothed before performing the difference to reveal only the large-scale (>10,000 km) circulation features. Although certain aspects of the map are probably unrealistic, based on comparison with dynamic height maps from hydrography, gyres with the correct sense are found in the major ocean basins. A strong Antarctic Circumpolar Current is also apparent. [From Cheney and Marsh (1982).]

ability of future geoid models and orbit determination techniques to improve this picture of the basin-scale circulation will be a demanding test of their absoute accuracy.

VIII. Wind Speed and Sea State

In addition to measuring sea surface topography and its temporal variations, information about sea surface conditions can be extracted from radar altimeter data. As the radar pulse reflects off an area of sea surface several kilometers in diameter, its shape changes because of the differences in distance between the satellite and the crests/troughs of surface waves which have characteristic wavelengths of 50–300 m. Also, during the reflection, a portion of the energy is scattered by ripples on the sea surface with wavelengths greater than several centimeters. Thus, three distinct properties of the reflected radar pulse, travel time, pulse shape and pulse amplitude, provide information about sea surface topography, sea surface waves and sea surface roughness, respectively.

Spatial variations in sea state and wind speed have been mapped from data acquired by both the GEOS-3 and SEASAT altimeters. The SEASAT maps reveal a number of new and interesting features of the global sea state and wind speed patterns during the period, 28 June 1978 to 10 October 1978 (Chelton *et al.*, 1981). Moreover, a detailed study of these data over the southern ocean shows that regions of high winds and waves migrate in longitude around Antarctica (Mognard *et al.*, 1983). These results from the SEASAT mission indicate that future altimetric satellites will provide more detailed information about sea surface conditions.

While SEASAT was highly successful in mapping the global distribution of sea state and wind speed, it was unable to recover much information about their temporal variations, because of its short lifespan. Undoubtedly, the largest time variations have a period of 1 yr. To obtain a reliable estimate of the seasonal variation, these quantities must be measured for a number of years.

The GEOS-3 altimeter, launched in April 1975, operated for nearly 4 years (April 1975–December 1978) and collected wave height and wind speed information intermittently during this time. A limitation of the GEOS-3 altimeter was that it could not store its data between times of ground communication. Therefore the geographical distribution of GEOS-3 data is very non-uniform when compared with the later SEASAT altimeter which carried a tape recorder. The GEOS-3 data density is highest near tracking stations and lowest in more remote areas of the world. Despite this relatively poor data distribution, averaging the GEOS-3 data over both space and

time reveals significant seasonal variation in wind speed and sea state. Moreover, the maps derived from the GEOS-3 data (Sandwell and Agreen, 1984) show substantial hemispherical asymmetry in the seasonal variations in these quantities. Most of the seasonal variation occurs in the Northern Hemisphere while winds and waves in the Southern Hemisphere are fairly steady.

During the austral winter (June–September) the largest wind speeds of 8–12 m/s occur in the Southern Hemisphere between latitudes of 40° and 60°. This band of high wind speed, which also appears on the SEASAT-derived maps (Chelton *et al.*, 1981; Mognard *et al.*, 1983), surrounds the Antarctic continent and is associated with mid-latitude winter storms. Highest average wind speeds (>10 m/s) generally occur away from continents and are centered over the Antarctic Circumpolar Current. Other more localized areas of high wind speed appear in the North Atlantic, the Gulf of Alaska, south of the Baja California Peninsula and in the Bay of Bengal. The latter feature is associated with monsoons. As noted by Chelton *et al.* (1981), both the North Atlantic and North Pacific are characterized by light winds during boreal summer.

The patterns of wind speed change drastically between summer and winter. As expected, wind speeds are very high in the North Atlantic and North Pacific during their winter. Indeed, the highest average wind speeds (>14 m/s) in the world's oceans occur in the northern North Atlantic during this period. It is interesting that there is not a complementary decrease in Southern Hemisphere wind speeds between the austral winter and summer.

GEOS-3 wind speed maps show zonal wind patterns that sailors have known about for centuries. These are the westerlies, the horse latitudes, the trades and the doldrums. To enhance these zonal wind speed patterns and their seasonal variations, the data were averaged into latitudinal zones. The results are shown in Fig. 15, where average wind speed for each seasonal period is plotted as a function of latitude. The zonal wind patterns are evident as local maxima and minima in this figure. The 5°–10° shift in the zonal patterns between the two seasonal periods is also apparent. The most striking feature of the zonal wind patterns is the large asymmetry in the summer-to-winter wind speed variation between the two hemispheres. In particular, the westerlies in the Northern Hemisphere increase by approximately 50% between summer and winter whereas the corresponding increase in the Southern Hemisphere is only 10%.

The global distribution of significant wave height and its seasonal variation is perhaps less well known, especially in the southern ocean. Since waves are generated by winds, one would expect a high correlation between wind speed and $H_{1/3}$. During boreal summer, average wave heights are low (2–3 m) in both the North Atlantic and North Pacific. In the southern oceans

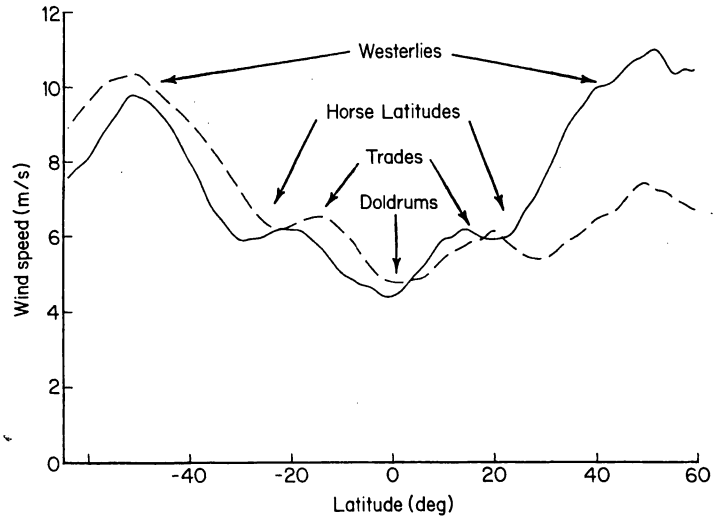

Fig. 15. Wind speed averaged over longitude for two seasonal periods, June–Sepember (dashed curve) and December–March (solid curve). The major zonal wind patterns shift between the two seasons.

significant wave heights are highest (4–5.5 m) during this period. Wave heights are generally low in equatorial regions because of low wind speeds in these areas.

The significant wave height map (see Sandwell and Agreen, 1984) for boreal winter shows a dramatic increase in $H_{1/3}$ in the northern ocean areas and only a small decrease in the southern oceans. This reflects the seasonal variation in wind speed. Like the average wind speed, the highest waves (>5.5 m) occur in the North Atlantic during its winter. Localized wave height maxima occur over the Kuroshio and Gulf Stream as well.

The zonal wave patterns are illustrated in Fig. 16 where longitudinally averaged significant wave height is plotted against latitude. The dominant zonal wave patterns are associated with the westerlies and therefore occur at mid-latitudes. Again note the dramatic seasonal change in the Northern Hemisphere while the seasonal variation in the Southern Hemisphere is relatively small. There is no pronounced local minimum corresponding to the horse latitudes although a hint of minimum appears at +20° on the December–March profile. The trade winds do not produce a local maximum in the zonal wave heights. There is, however, a wave height minimum corresponding to the doldrums. Moreover, this minimum shifts by about 5–10° between the two seasonal periods reflecting the shift in the zonal wind patterns.

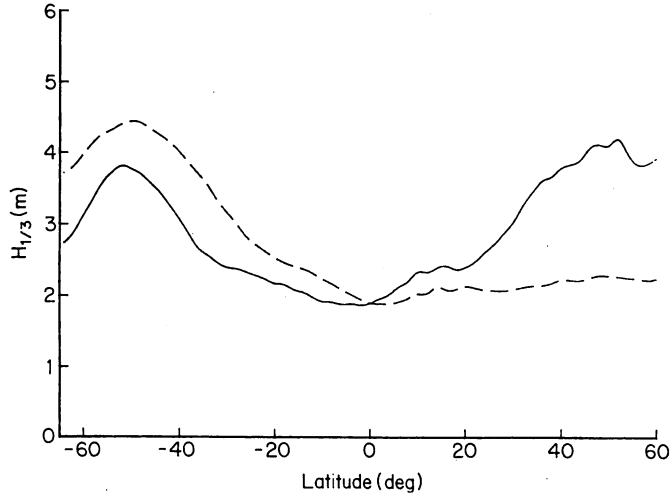

Fig. 16. Significant wave height averaged over longitude for the two seasonal periods, June–September (dashed curve) and December–March (solid curve). Wave propagation smooths the zonal wave patterns with respect to the zonal wind patterns.

The smoothness of the zonal wave patterns as compared with the zonal wind patterns is due to wave propagation. Waves generated by storms in the mid and high latitudes propagate to lower latitudes where they are detected by the altimeter (Mognard, 1982). This propagation effect is most apparent on the December–March map where the central ocean areas, with their large aperture of exposure, have higher waves than coastal areas where waves can approach from only one side.

Acknowledgments

The authors gratefully acknowledge the U.S. Government to reproduce the figures in this chapter.

References

Brown, O. B. and Cheney, R. E. (1983). Advances in satellite oceanography, *Rev. Phys. Space Phys.* **21** (5), 1216–1230.

Chapman, M. E. (1979). Techniques for interpretation of geoid anomalies, *J. Geophys. Res.* **84**, 3793–3901.

Chelton, D. B., Hussey, K. J. and Parke, M. E. (1981). Global satellite measurements of water vapor, wind speed and wave height, *Nature* **294**, 529–532.

Cheney, R. E. and Marsh, J. G. (1982). Global ocean circulation from satellite altimetry. *Trans. Am. Geophys. Un.* **63**, 997.

Cheney, R. E., Marsh, J. G. and Beckley, B. D. (1983). Global mesoscale variability from collinear tracks of SEASAT altimeter data. *J. Geophys. Res.* **88**(C7), 4343-4354.

Crough, S. T. and Jurdy, D. M. (1980). Subducted lithosphere, hot spots and the geoid. *Earth Planet Sci. Lett.* **48**, 15-22.

Douglas, B. C., Cheney, R. E. and Agreen, R. W. (1983). Eddy energy of the northwest Atlantic and Gulf of Mexico determined from GEOS-3 altimetry. *J. Geophys. Res.* **88**(C14), 9595-9603.

Douglas, B. C., Agreen, R. W. and Sandwell, D. T. (1984). Observing global ocean circulation with SEASAT altimeter data. *Mar. Geod.* **8**, 67-83.

Engelis, T. (1983). Analysis of sea surface topography using SEASAT altimeter data. Rep. 343, Dep. of Geodetic Science and Surveying, Ohio State Univ., Columbus, Ohio.

Fedor, L. S., Godbey, T. W., Gower, J. F. R., Guptill, R., Hayne, G. S., Rufenach, C. L. and Walsh, E. J. (1979). Satellite altimeter measurements of sea state—An algorithm comparison. *J. Geophys. Res.* **84**, 3991-4001.

Griggs, D. T. (1972). The sinking lithosphere and the focal mechanisms of deep earthquakes. In "The Nature of the Solid Earth" (E. C. Robertson, ed.) pp. 361-384, McGraw-Hill, New York.

Hager, B. H. (1984). Subducted slabs and the geoid: constraints on mantle rheology and flow. *J. Geophys. Res.* **89**, 6003-6015.

Haxby, W. F., and Turcotte, D. L. (1978). On isostatic geoid anomalies. *J. Geophys. Res.* **83**, 5473-5478.

Lerch, F. J., Marsh, J. G., Klosko, S. M., and Williamson, R. G. (1982). Gravity model improvement for SEASAT. *J. Geophys. Res.* **87**, 3281-3296.

Levitus, S. (1982). Climatological atlas of the world ocean. NOAA Professional Paper 13 Rockville, Maryland.

Marsh, J. G. and Martin, T. V. (1982). The SEASAT altimeter mean sea surface model. *J. Geophys. Res.* **87**, 3269-3280.

Marsh, J. G. and Williamson, R. G. (1980). Precision orbit analyses in support of the SEASAT saltimeter experiment. *J. Astron. Sci.* **28**, (4), 345-369.

McAdoo, D. C. and Martin, C. F. (1984). SEASAT observations of lithospheric flexure seaward of trenches. *J. Geophys. Res.* **81**, 3201-3210.

McAdoo, D. C., Martin, C. F. and Poulose, S. (1985). SEASAT observations of flexure: Evidence for a strong lithosphere. *Tectonophysics.* **116**, 209-222.

Menard, Y. (1983). Observations of eddy fields in the northwest Atlantic and northwest Pacific by SEASAT altimeter data. *J. Geophys. Res.* **86**, 8022-8030.

Mognard, N. M. (1982). Applications of satellite radar altimetry to the determination of sea state. Thesis, University Paul Sabatier de Toulouse, Toulouse, France.

Mognard, N. M., Campbell, W. J., Cheney, R. E. and Marsh, J. G. (1983). Southern ocean mean monthly waves and surface winds for winter 1978 by SEASAT radar altimeter. *J. Geophys. Res.* **88**, 1736-1744.

National Aeronautics and Space Administration (1981). Satellite altimetric measurements of the ocean: Report of the TOPEX science working group. Jet Propulsion Laboratory, Pasadena, California.

Parsons, B. and Sclater, J. G. (1977). An analysis of the variation of ocean floor bathymetry with age. *J. Geophys. Res.* **82**, 803-827.

Sandwell, D. T. (1984). Thermomechanical evolution of oceanic fracture zones. *J. Geophys. Res.* **89**, 11401-11413.

Sandwell, D. T. and Agreen, R. W. (1984). Seasonal variation in wind speed and sea state from global satellite measurements, *J. Geophys. Res.* **89**.

Sandwell, D. T. and Schubert, G. (1982). Lithospheric flexure at fracture zones. *J. Geophys. Res.* **87**, 4657-4667.

Schwiderski, E. W. (1979). Ocean Tides, Part I: Global ocean tidal equations. *Mar. Geod.* **3**, 161-217.

Tai, C. K. and Wunsch, C. (1983). Absolute measurement by satellite altimetry of dynamic topography of the Pacific Ocean. *Nature* **301**, 408-410.

Tai, C. K. and Wunsch, C. (1984). An estimate of global absolute dynamic topography, *J. Phys. Oceanogr.* **14** (2), 457-463.

Vening-Meinesz, F. A. (1964) "The Earth's Crust and Mantle", p. 124. Elsevier, New York.

Wagner, C. A. and Lerch, F. J. (1978). The accuracy of geopotential models. *Planet. Space Sci.* **26**, 1081-1140.

Watts, A. B. and Ribe, N. W. (1984). On geoid heights and flexure of the lithosphere at seamounts. *J. Geophys. Res.* **89**, 11152-11170.

Watts, A. B. and Talwani, M. (1974). Gravity anomalies seaward of deep-sea trenches and their tectonic implications. *Geophys. J. R. Astron. Soc.* **36**, 57-90.

Wilson, J. T. (1965). A new class of faults and their bearing on continental drift. *Nature* **207**, 343-347.

Wyrtki, K. (1979). Sea level variations; monitoring the breath of the Pacific. *EOS*, **60**(3), 25-27.

Wyrtki, K. (1985). Monthly maps of sea level in the Pacific during the El Niño of 1982 and 1983. *IOC Tech. Ser. 30*, UNESCO, Paris.